

Surface alloying and iron selenide formation in Fe/Bi₂Se₃(0001) observed by x-ray absorption fine structure experiments

A. Polyakov,¹ Holger L. Meyerheim,¹ E. Daryl Crozier,² R. A. Gordon,² K. Mohseni,¹ S. Roy,¹ A. Ernst,¹ M. G. Vergniory,^{1,3} X. Zubizarreta,¹ M. M. Otrokov,^{3,4} E. V. Chulkov,^{3,4,5,6} and J. Kirschner¹

¹Max-Planck-Institut für Mikrostrukturphysik, Weinberg 2, D-06120 Halle, Germany

²Department of Physics, Simon Fraser University, Burnaby, British Columbia, Canada V5A 1S6

³Donostia International Physics Center (DIPC), 20018 San Sebastián/Donostia, Basque Country, Spain

⁴Tomsk State University, 634050 Tomsk, Russia

⁵Departamento de Física de Materiales UPV/EHU, Centro de Física de Materiales CFM - MPC and Centro Mixto CSIC-UPV/EHU, 20080 San Sebastián/Donostia, Basque Country, Spain

⁶Saint Petersburg State University, Saint Petersburg 198504, Russia

(Received 28 May 2015; published 22 July 2015)

The atomic structure of ultrathin iron films deposited on the (0001) surface of the topological insulator Bi₂Se₃ is analyzed by surface x-ray absorption spectroscopy. Iron atoms deposited on a Bi₂Se₃ (0001) surface kept at 160 K substitute bismuth atoms within the first quintuple layer. Iron atoms are neighbored by six selenium atoms at a distance in the 2.4 Å range indicating substantial atomic relaxations. Mild annealing up to 520 K leads to the formation of α -FeSe, characterized by a local order extending up to the sixth shell (5.80 Å). *Ab initio* calculations predict a noncollinear magnetic ordering with a transition temperature of 3.5–10 K depending on the iron concentration and the number of the layers in which Fe is located.

DOI: [10.1103/PhysRevB.92.045423](https://doi.org/10.1103/PhysRevB.92.045423)

PACS number(s): 61.05.cp, 71.15.Mb, 73.20.At, 79.60.−i

I. INTRODUCTION

Topological insulators (TIs) have been under focus in contemporary condensed matters physics research [1–3]. Although semiconductors in the bulk, they host a gapless, linearly dispersing state at the surface, which is a consequence of strong spin-orbit coupling. The hallmark of this so-called topological surface state is a helical spin texture that protects surface electrons from backscattering on defects as long as time reversal symmetry is preserved [4,5]. Such a property makes TIs a unique playground for observation of new effects and apart from the pristine TI surfaces [6–9], the TIs covered with various overlayers [10–12] or adsorbates [13–20] have also been studied intensely.

In particular, the deposition of magnetic atoms at TI surfaces is of great interest as an approach to study the interplay of magnetism and topological surface state [21,22]. The onset of an out-of-plane ferromagnetic (FM) order in a system of adatoms at a TI surface is expected to break time reversal symmetry whereupon the topological surface state must split. Such a behavior is confirmed by recent *ab initio* calculations [23–25]. However from the experimental side there is an ongoing discussion regarding whether the doping of a TI surface with magnetic atoms leads to an opening of a gap at the Dirac point [16,18,26–28]. While the Dirac point splitting at Bi₂Se₃(0001) upon iron deposition was initially reported in [16], subsequent angle-resolved photoemission spectroscopy (ARPES) studies did not find evidence of the magnetic adsorbate-induced gap opening [18,26–28]. Accordingly, magnetic measurements found no evidence of the long-range FM order in the systems of Fe and Co adatoms at the Bi₂Te₃ [29] and Bi₂Se₃ [19,26,30] surfaces (the coverage in the latter case was reaching 0.9 monolayers).

Interpretation of these magnetic and photoemission measurements requires detailed knowledge of the near surface atomic structure, i.e., localization and distribution of the

adsorbate. These, in turn, depend crucially on such experimental conditions as deposition and annealing temperatures. To date, the low-temperature deposition case without subsequent annealing, when the diffusion below the surface appears hardly probable, is quite well understood for individual iron adatoms on Bi₂Se₃(0001). Combined STM and *ab initio* studies point out the surface hollow sites (fcc and hcp) as the most favorable ones for the iron coverage of ~ 0.01 monolayers (ML) [19,27]. By contrast, for the thermally activated case (high-temperature deposition or annealing) the subsurface substitutional sites, Fe_{Bi}, have been proposed for iron-deposited Bi₂Se₃ [27] and Bi₂Te₃ [31] by combined APRES, STM, and *ab initio* studies. Note that the situation here is somewhat similar to the bulk doped Bi₂Se₃ case in which iron atoms are known to predominantly substitute Bi [32,33]. In the just mentioned STM studies [32,33] the interstitial [32,33] and van der Waals [33] iron positions in the bulk Bi₂Se₃ have also been identified. These scenarios in principle should be considered as well in the case of thermally activated penetration of the adsorbates in the bulk. Finally, the annealing temperatures for the systems under discussion typically do not exceed 370 K [27,31]. Thus, there is hardly any information available on what happens when the iron-deposited Bi₂Se₃ surface is annealed at significantly higher temperatures.

This situation calls for a further analysis of the near surface structure of iron-deposited Bi₂Se₃(0001). To this end we have carried out x-ray absorption fine structure (XAFS) measurements above the Fe-K edge, the analysis of which suggests that iron atoms occupy bismuth substitutional sites when deposited at a temperature as low as 160 K. No indication of iron atoms located in the interstitials of the topmost quintuple layer (QL) block or inside van der Waals (vdW) gap is observed. Moreover, we find that annealing up to 520 K for several minutes results in the formation of a local α -FeSe structure. The experimentally obtained structural information is further utilized in a first-principles study on

magnetic properties of Fe/Bi₂Se₃(0001) within the density functional theory.

II. EXPERIMENT

X-ray absorption fine structure (XAFS) measurements were carried out at the insertion device beamline 20 at the Advanced Photon Source (APS), Argonne National Laboratory (USA), using the MBE1 end station [34] equipped with standard surface analytical tools. The (0001) surface of the single Bi₂Se₃ crystal was cleaned by mild argon ion sputtering (1 keV) followed by annealing up to approximately 800 K. The surface cleanliness was checked by Auger-electron spectroscopy (AES). No traces of carbon and other impurities were observed.

Subsequently Fe was deposited *in situ* by molecular beam epitaxy from an iron rod (99.999% Fe) heated by electron bombardment. During deposition and data collection the substrate temperature was kept in the range between 155 and 170 K (designated henceforth as 160 K). The film thickness was estimated by considering the ratios between the AES peak-to-peak intensities of the Fe-LMM (651 eV), the Bi-NOO (101 eV), and the Se-MMM (43 eV) Coster-Kronig transitions.

III. XAFS ANALYSIS

A. Iron on Bi₂Se₃(0001)

The XAFS experiments were carried out after depositing approximately 0.3 ML iron, above the Fe-K absorption edge ($E_0 = 7112$ eV) in the fluorescent yield (FY) mode using a 4-element vortex Si-drift detector. Here and in the following 1 ML is equal to 6.74×10^{14} atoms/cm². Monochromatic x rays from a Si(111) double-crystal monochromator, with the 7 GeV APS ring operating in top-up mode, were incident on the substrate at approximately 2/3 of the critical angle ($\alpha_c \approx 0.4$) for total reflection to avoid errors due to anomalous dispersion effects [35]. The in-plane and out-of-plane Fe atomic environment was investigated exploiting the polarization dependence of the linearly polarized x-ray beam with the electric field vector aligned either perpendicular (E_{\perp}) or parallel (E_{\parallel}) to the substrate surface.

Figure 1 shows the photon energy (E) dependence of the ratio (R) between the FY and the primary beam intensity (I_0) normalized to the edge jump. R is proportional to the linear absorption coefficient, $\mu(E)$. Red and blue lines correspond to $\mu(E)$ collected using the E_{\parallel} and E_{\perp} geometry, respectively. The k^2 -weighted EXAFS interference functions, $\chi(k)$, extracted from the FY data using the program ATHENA [36,37], are shown in the inset. The $\chi(k)$ function is given by $\chi(k) = [\mu(k) - \mu_0(k)]/\mu_0(k)$, where $\mu_0(k)$ represents the continuous atomic background and k the photoelectron wave vector, which is given by $k = \sqrt{2m(E - E_0)}/\hbar$. Direct inspection of both $\mu(E)$ and $\chi(k)$ clearly indicates the absence of any polarization dependence in the EXAFS signal and the dominance of a single frequency, i.e., of one neighbor shell [see also the Fourier transform (FT) in Fig. 3, below]. Anisotropic surface sites such as the “hcp” or the “fcc” hollow site as well as the selenium substitution or a vdW gap site would involve a strong polarization dependence of $\chi(k)$. In consequence they can directly be excluded as will be shown in the following.

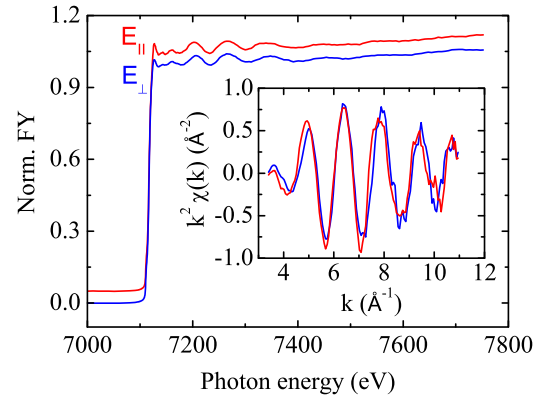


FIG. 1. (Color online) X-ray absorption spectra for approximately 0.3 ML iron on Bi₂Se₃(0001) collected using E_{\parallel} (red) and E_{\perp} (blue) polarizations. Spectra are normalized to the edge jump and shifted for clarity. The inset shows the corresponding k^2 -weighted $\chi(k)$ functions.

The near surface structure of Bi₂Se₃ is schematically shown in Fig. 2. The Bi₂Se₃ crystal structure is characterized by a stack of vdW-bonded QLs each being composed of a Se-Bi-Se-Bi-Se sequence of layers. Possible localizations of iron atoms (light gray) are labeled by “fcc”, “hcp”, “gap”, (bismuth) “substitutional”, and “interstitial”. The polarization dependence of the $\chi(k)$ function can be calculated by using the expression of the effective coordination number N_i^* of the i th shell around the absorber which is given by

$$N_i^* = 3 \times \sum_{j=1}^N \cos^2(\alpha_{ij}), \quad (1)$$

in which α_{ij} represents the angle between electric field vector E and the vector between the absorber i and the backscatterer j , where the summation extends over all atoms j of the shell. The effective coordination number N^* contributes to

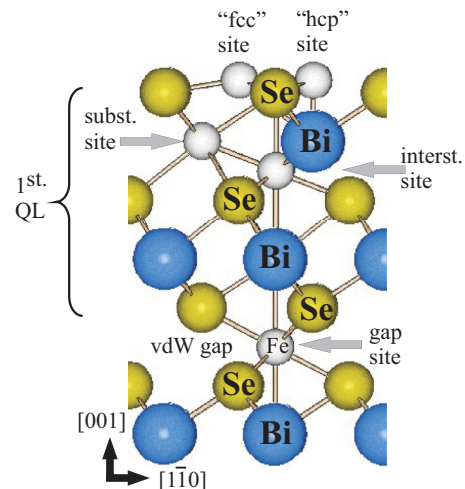


FIG. 2. (Color online) Schematic view of adsorption sites for iron on Bi₂Se₃(0001). Bismuth and selenium atoms are shown as large blue and small yellow spheres, respectively. Iron is represented by light gray balls. High symmetry adsorption sites of iron are indicated.

TABLE I. Effective coordination numbers N^* for different adsorption sites shown in Fig. 3.

Site	R_1	R_2	$N_{1\parallel}^*$	$N_{2\parallel}^*$	$N_{1\perp}^*$	$N_{2\perp}^*$
fcc	2.42 (Se)	3.09 (Bi)	4.39	2.69	0.23	3.63
hcp	1.96 (Bi)	2.42 (Se)	0.00	4.39	3.00	0.23
gap	2.71 (Se)	2.85 (Bi)	7.02	0.00	3.96	6.00
subst.	2.86 (Se)	3.07 (Se)	3.13	2.73	2.75	3.54
inters.	2.58 (Se)	2.58 (Bi)	3.87	3.87	1.26	1.26

the EXAFS amplitude, which is part of the general EXAFS equation:

$$\chi(k) = \sum_i \frac{S_0^2 N_i^* F_i(k)}{k R_i^2} e^{(-2k^2 \sigma_i^2)} e^{(-2R_i/\lambda_i)} \sin[2k R_i + \delta_i(k)], \quad (2)$$

with backscattering amplitudes $F_i(k)$, mean-free-paths (λ_i), and phase shifts $\delta_i(k)$ generated by the FEFF7 program [38]. The parameter S_0^2 describes the effect the relaxation of the $(N-1)$ “passive” electrons has on the EXAFS amplitude after the photoelectron is emitted [39,40]. The remaining parameters N_i^* (effective coordination number), R_i (distance), and σ_i^2 (mean-square relative displacement) are available to be fitted as will be discussed below. Following Eq. (1), Table I provides an overview of the calculated values of N^* for the different adsorption sites.

In calculating N^* for the “fcc” and the “hcp” sites it was assumed that iron adsorbs at such a height above the surface that the Fe-Se interatomic distance lies close to 2.4 Å which is commonly observed for Fe-Se distances such as in bulk α -FeSe (2.38 Å) [41,42]. While for the “fcc” site this gives a quite reasonable second-shell distance of $R_2 = 3.09$ Å for the neighboring bismuth atom in the second layer, in the case of the “hcp” site this scenario would involve an unphysical short distance of 1.96 Å to the bismuth atom directly underneath. In addition, for both sites a strong polarization dependence of N^* would be observed, which is in clear contrast to the experimental observation. Moreover we note that, whenever bismuth would be involved in the backscattering, it would be observable by the strong k dependence of its backscattering amplitude $F_{\text{Bi}}(k)$ characteristic for heavy elements (Ramsauer-Townsend effect). Our model calculations for these sites (not shown) have proven that an additional peak appears in the FT as a consequence of the $F_{\text{Bi}}(k)$ modulation.

With the same arguments outlined for the “fcc” and the “hcp” site also the “gap” and the interstitial site can be ruled out. For the former, excluding relaxations the Fe-Se distance is equal to 2.71 Å and 2.85 Å for the Fe-Bi distance. Also in this site a strong polarization dependence should be observed.

The only adsorption site which fits all observations, as a polarization-independent $\chi(k)$ function characterized by a single frequency, is the bismuth substitutional site. Neglecting structural relaxations also for this site, the iron atom is neighbored by two closely spaced shells of selenium atoms at a distance of $R_1 = 2.87$ Å and $R_2 = 3.07$ Å. For this unrelaxed geometry, there is a small polarization dependence of the effective coordination number (see Table I), which, however, nearly cancels out if the two shells are considered as

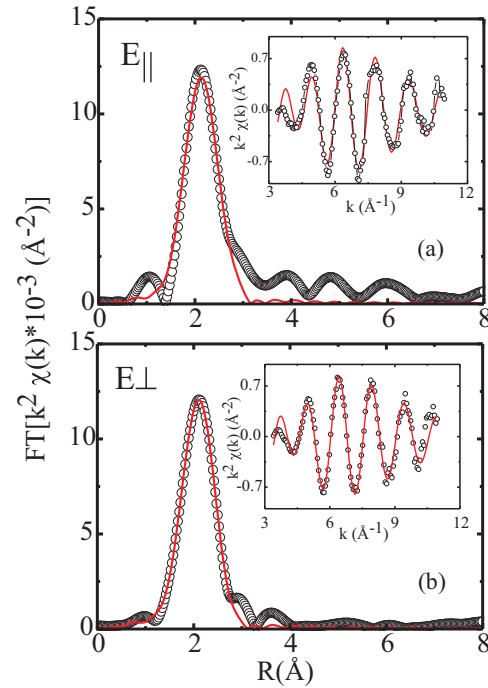


FIG. 3. (Color online) Experimental (symbols) and calculated (lines) magnitude of the Fourier transforms of the k^2 -weighted $\chi(k)$ functions for E_{\parallel} (a) and E_{\perp} (b). The inset shows the corresponding k^2 -weighted $\chi(k)$ functions. No polarization dependence is observable.

a single one ($N_{\parallel}^* = 5.86$ versus $N_{\perp}^* = 6.29$). In summary, from the qualitative analysis it can be concluded that iron atoms substitute bismuth atoms. We suggest that at 160 K deposition temperature substitution takes place predominantly in the top QL, since diffusion across the vdW gap at this temperature appears as kinetically unfavorable.

The qualitative result is confirmed by the quantitative analysis based on curve fitting. Fourier transforms (FTs) of the $k^2\chi(k)$ functions were calculated for each spectrum by using a 20% Gaussian window function in the WinXAS code [44]. The k range used for the FT integration extends from $k_{\min} = 3.38$ Å⁻¹ to $k_{\max} = 11.02$ Å⁻¹. Figure 3 compares the magnitudes of the FTs derived for the E_{\parallel} (a) and the E_{\perp} (b) geometries. The insets show the k^2 -weighted $\chi(k)$ functions. Experimental data are represented by symbols, fitted curves by red lines.

Fitting of the EXAFS data was carried out in real space over a range 1.3 to 2.8 Å using model amplitudes and phases generated by FEFF7 implemented in the WinXAS program [44]. This minimizes any influence of multiple-scattering contributions and higher shells leaking into the first peak. The fit results are summarized in Table II listing the fit parameters obtained for a two-shell (upper panel) and one-shell (lower panel) model, respectively. In general, a slightly better fit based on the unweighted residual (R_u) [43] is obtained for the two-shell models. The environment is characterized by a shell of six selenium atoms, where the minimum and maximum distance is equal to 2.39 Å and 2.57 Å, respectively. The fitted values for the mean-squared relative displacement amplitude (MSRD) are about a factor of 2 larger for the case of the one-shell model ($\sigma^2 = 0.012$ Å² versus $\sigma^2 = 0.006$ Å²)

TABLE II. Table of structural parameters for 0.3 ML Fe on Bi_2Se_3 . The meaning of the parameters is as follows: R = nearest neighbor distance, N^* = effective coordination number, σ^2 = mean-squared relative displacement amplitude, ΔE_0 = shift of absorption edge, R_u = residual [43]. The amplitude reduction factor (S_0^2) was kept constant at $S_0^2 = 0.67$ in all cases. Parameters labeled by an asterisk (*) are kept fixed. Two kinds of models were used, one employing a two-shell fit, the second using one selenium shell only. Uncertainties are given in parentheses. They are estimated on the basis of the variance of the residuum upon variation of the parameter allowing all other parameters to vary.

Geometry	R_1 (Å)	N_1^*	σ_1^2 (Å ²)	E_0 (eV)	R_2 (Å)	N_2^*	σ_2^2 (Å ²)	E_0 (eV)	R_u
E_{\parallel}	2.42(3)	3.00(*)	0.005(1)	2.6(4)	2.57(3)	3.00(*)	0.007(1)	8.0(4)	0.065
E_{\perp}	2.39(3)	3.00(*)	0.006(1)	1.8(6)	2.52(3)	3.00(*)	0.009(1)	7.6(2)	0.020
E_{\parallel}	2.46(3)	6.00(*)	0.011(1)	2.0(4)					0.087
E_{\perp}	2.43(3)	6.00(*)	0.012(1)	0.9(1)					0.030

indicating the dispersion of the neighbor distance. We note that the amplitude reduction factor ($S_0^2 = 0.67$) was derived from an α -FeSe powder sample measured in transmission mode and fitting the first two neighbor shells as outlined below.

Comparison of the fitted neighbor distances and the calculated ones assuming an unrelaxed host lattice (approximately 2.4 to 2.6 Å versus to 2.86 and 3.08 Å) indicates substantial relaxation of the selenium neighbors of approximately 0.4 Å upon bismuth substitution by iron. This is attributed to the smaller size of the iron atom, which manifests itself in a shorter equilibrium Fe-Se bond length of 2.38 Å as in α -FeSe. Previous experimental and theoretical investigations dealing with 3d transition metal (TM) doped Bi_2Se_3 alloy films are in excellent quantitative agreement with our results [45–48]. The first-principles calculations of Abdalla *et al.* [46] in general favor the bismuth substitutional site for iron, manganese, and chromium over other sites such as the hcp or the fcc site discussed above. In detail for the (bismuth) substitutional site Fe-Se equilibrium distances of 2.54 and 2.82 Å are predicted. While these theoretical values are somewhat too large as compared to our results, recent x-ray spectroscopy experiments carried out for chromium-doped Bi_2Se_3 by Liu *et al.* [48] and by Figueroa *et al.* [48] have revealed distances between 2.50 and 2.64 Å, the latter for a two-shell model similar to ours.

In summary, we conclude that there is a strong tendency for iron to replace bismuth which takes place even at 160 K, i.e., well below room temperature which can be seen as the beginning of an interface reaction to form iron selenide. As will be shown below mild annealing induces the formation of a locally ordered α -FeSe-like phase.

B. Thermally annealed iron on $\text{Bi}_2\text{Se}_3(0001)$

In a second experiment the as-deposited sample was subject to mild annealing up to 520 K for several minutes. XAFS experiments were carried out after the sample was cooled down to 160 K. Upon annealing dramatic modifications of the absorption signal are observed indicating the formation of α -FeSe as outlined in the following. In this context it is important to note that the α -FeSe phase belongs to the class of pnictide superconductors and its structure is the most simple one in this class [41]. Consequently, many attempts have been made to prepare ultrathin films of α -FeSe by molecular beam epitaxy on suitable substrates in order to study its superconducting properties and to increase the

superconducting transition temperature T_C ($T_C = 8$ K in bulk α -FeSe) [50–52]. Our approach to simply anneal a Bi_2Se_3 crystal covered by an iron film in submonolayer to monolayer thickness range can be seen as a simple technique to prepare the α -FeSe phase. A more detailed discussion will be presented elsewhere [53,54].

At first we discuss the near edge structure. Figure 4 shows several x-ray absorption near edge spectra (XANES) in the vicinity of the Fe-K edge. They are labeled by (1) to (6) and are vertically shifted for clarity. Solid lines (1, 2, and 6) correspond to spectra collected from our samples while those shown by dashed lines (3, 4, and 5) are reproduced from Ref. [49]. For the latter case hydrostatic pressure (0.0, 4.2, and 11.8 GPa) was exerted on bulk powder samples using a diamond anvil cell. All spectra are characterized by three features, labeled as A, B, and C. According to Ref. [49] the pre-edge feature A, which exhibits a pronounced pressure dependence, is related to the $1s$ to $3d$ quadrupole transition and to the dipole transition between the $1s$ initial state and the Fe $3d$ –Se $4p$ hybrid orbitals. A pressure dependence is also observed for the features B and C, attributed to multiple scattering from atoms in the vicinity of iron. The spectrum of our annealed sample (6) bears several

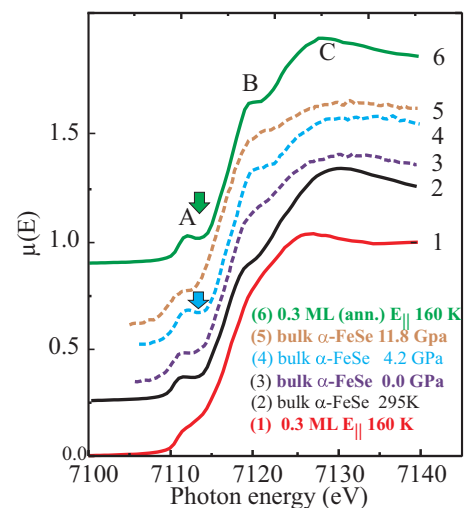


FIG. 4. (Color online) Fe-K-edge XANES spectra of 0.3 ML Fe/ Bi_2Se_3 collected in E_{\parallel} geometry (1) compared with that of a bulk α -FeSe powder (2) and of the 520 K annealed sample (6). Spectra plotted by dashed lines (3, 4, 5) are reproduced from Ref. [49] emphasizing the pressure dependence of the XANES.

resemblances with spectrum collected under 4.2 GPa pressure (4). Notably, both spectra show a local minimum (emphasized by arrows) at the high-energy side of feature A, which is not present in the spectra of all other samples.

Similarly, feature B has also a maximum at 4.2 GPa (4) similar to that of the annealed sample (6). At ambient pressure (spectrum 3) and at 11.8 GPa (5) both features A and B are less pronounced. We conclude that annealing of the as-deposited iron film leads to the formation of a local α -FeSe phase which is under considerable compressive strain resulting from coherent epitaxial growth [54]. We also note that regarding peak C some differences exist between the spectra of our samples and those shown in Ref. [49], where it is less pronounced. A direct comparison between spectrum 2 and 3 corresponding to our bulk powder α -FeSe sample and the reference sample

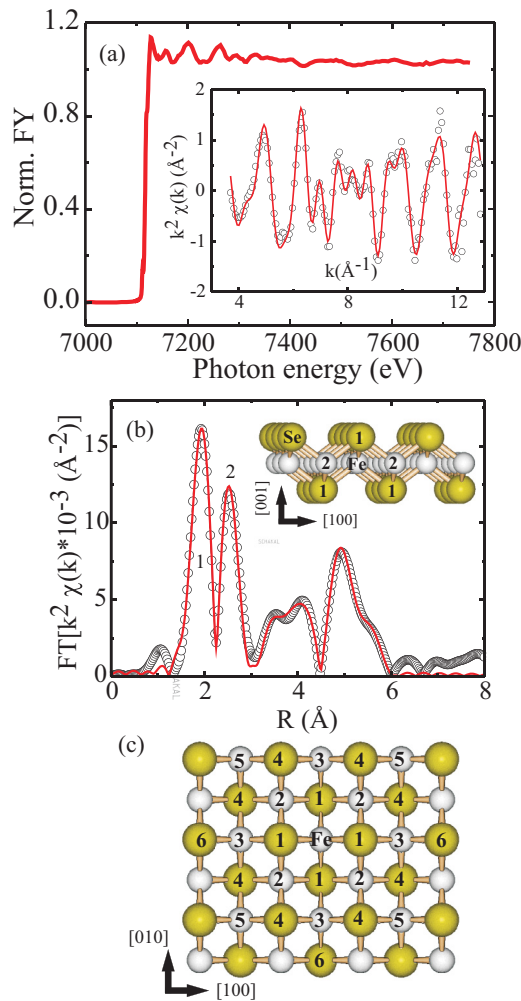


FIG. 5. (Color online) (a) Fe-K EXAFS measured at 160 K on the 0.3 ML Fe/Bi₂Se₃ sample after annealing at 520 K. The inset shows the k^2 -weighted $\chi(k)$ function (symbols: experiment; fit: lines). (b) Corresponding magnitude of the FT. The inset shows a side view of one Se-Fe-Se triple layer, where labels “1” and “2” indicate the first (Se) and second (Fe) neighbor shell corresponding to the first and second FT maximum, respectively. (c) Structure model for one Se-Fe-Se triple layer. Labels i with $i = 1, 2, \dots, 6$ indicate neighbor shells taken into account in the fitting.

TABLE III. Structure parameters for α -FeSe. The left columns list values for the bulk phase. The right columns (FIT) represent fit results to the sample at 160 K. Parameters labeled with * are kept constant. The parameter S_0^2 was kept constant at 0.67. Uncertainties are given in parentheses. The residuum is equal to 0.067.

Shell	R_i^{bulk} (Å)	N_i^{bulk}	R_{FIT} (Å)	N_{FIT}^*	σ_{FIT}^2 (Å ²)	E_0 (eV)
Se(1)	2.38	4.0	2.39(2)	3.8(*)	0.003(1)	6.8(1)
Fe(2)	2.66	4.0	2.66(2)	6.0(*)	0.005(1)	8.6(1)
Fe(3)	3.77	4.0	3.78(3)	6.0(*)	0.013(3)	8.0(1)
Se(4)	4.46	8.0	4.46(3)	10.8(*)	0.010(3)	7.0(1)
Fe(5)	5.34	4.0	5.27(4)	6.0(*)	0.008(2)	-1.5(1)
Se(6)	5.84	4.0	5.86(5)	6.2(*)	0.006(2)	-0.3(2)

related to ambient pressure, respectively, makes this more evident. While we cannot make a conclusive statement about the reasons regarding this discrepancy we may speculate that the powder samples can contain some nonidentified phases.

In the next step the full EXAFS spectrum is analyzed. Figure 5(a) shows the absorption spectrum of the sample, while solid symbols in the inset represent the k^2 -weighted $\chi(k)$ function together with the calculated one (red solid line) based on the fit. The magnitude of the FT in Fig. 5(b) shows many peaks indicating a well-defined atomic order at least up to about 6 Å around the iron atom. We remind the reader that the experiment was carried out in the E_{\parallel} geometry; i.e., the EXAFS is most sensitive to the structure *within* a FeSe triple layer (TL). The structure of α -FeSe is characterized by TLs consisting of a Se-Fe-Se layer sequence, while the vdW-bonded TLs are stacked along [001]. One TL is schematically shown in the inset of Fig. 5(b). From scanning tunneling microscopy (STM) and surface x-ray diffraction experiments [53] it is concluded that FeSe nanocrystals are formed and embedded into the substrate crystal when ultrathin iron films are deposited on Bi₂Se₃(0001) and annealed afterwards. These nanocrystals which are up to several hundred nanometers in lateral size exhibit an epitaxial relationship to the trigonal two-dimensional unit cell of the substrate. They grow with their basal planes parallel to the (0001) plane of the substrate crystal and are about three TLs thick on average. The detailed EXAFS analysis indicates that the atomic structure of the annealed sample is close to α -FeSe as Table III lists neighbor shells around iron in α -FeSe. The first two columns list the neighbor distance R_i^{bulk} and the crystallographic coordination number (N_i^{bulk}) of the i th shell up to $i = 6$ in the bulk structure, while the rest list the fit results indicated by the subscript FIT.

In order to reduce the number of free fit parameters we have assumed a complete coordination for each shell. The effective coordination number, N_i^* , as calculated for the E_{\parallel} geometry is used for the fit as a constant parameter. Owing to the large size of the α -FeSe nanocrystals, the fraction of undercoordinated iron atoms at the island rims is negligible; thus the assumption of a complete coordination appears as justified. Only the distance R_i , the MSRD σ_i^2 , and the energy shift were allowed to vary. Figure 5(c) schematically shows the environment around an iron atom (here labeled by Fe) within a TL. Numbers 1 to 6 correspond to the neighbor shells according to Table III. The fit results are listed on the right. We

find that the difference between the bulk and the fitted distance is significant with $\Delta R = 0.07 \text{ \AA}$ only for $i = 5$ (5.27 \AA in the film versus 5.34 \AA in the bulk). We note that this shell is the only one which is affected by strong multiple scattering contribution by the intervening iron atom labeled by 2. All other parameters are within the normal range, except that the σ^2 for the third and fourth shell appear as somewhat enhanced as compared to previous EXAFS studies dealing with bulk $\text{FeSe}_{1-x}\text{Te}_x$ powder samples [45] or the chromium-doped films [48] where values in the range between 0.003 and 0.006 \AA^2 were derived.

IV. THEORY

The structural information obtained in the current experiments is used for further studies of magnetic properties of $\text{Fe/Bi}_2\text{Se}_3(0001)$ from first principles within the framework of the density functional theory. If the structure and the chemical composition of a studied system is known, first-principles methods can provide an adequate description for electronic and magnetic structures of real materials. For our study we have chosen a fully relativistic self-consistent Green's function method [55]. In this method, disorder effects are effectively treated by using the coherent potential approximation, which describes uniformly distributed impurities or defects without any short-range effects [56,57]. Two scenarios were considered: (i) iron replaces bismuth in the subsurface Bi layer only and (ii) iron replaces bismuth in both bismuth layers within the first QL. The aim of the calculations was to determine the type of iron magnetic ordering and its critical temperature.

In the previous study [58] bulk $\text{Bi}_{2-x}\text{Fe}_x\text{Se}_3$ was found to be an antiferromagnet (AF) with Néel temperature $T_N = 15 \text{ K}$ at $x = 0.2$. In this case each atomic layer, being AF ordered, is characterized by a very strong AF *intralayer* coupling ($J_1^{00} = -9.02 \text{ meV}$) between the nearest neighbor iron atoms. Here and in the following J_v^{ij} labels the exchange parameter between first ($v = 1$), second ($v = 2$), and so on nearest neighbor atoms in the first ($i = 0, j = 0$), second ($i = 1, j = 1$), or between the first and second bismuth layer ($i = 0, j = 1$), respectively (see inset of Fig. 6).

The *interlayer* interaction is also negative and not negligible: between the different $\text{Bi}_{2-x}\text{Fe}_x$ layers within a QL the exchange parameter is equal to $J_1^{01} = -8.12 \text{ meV}$ and even across the vdW gap it is equal to $J_1^{02} = -2.03 \text{ meV}$ and $J_2^{02} = -3.90 \text{ meV}$ [58]. The AF order has its origin in the strong localization of $3d$ impurity states combined with large exchange splitting.

In the present case, the magnetic structure is different from that of the bulk, since the iron atoms are located in the topmost QL only occupying substitutional sites in either one $\text{Bi}_{2-x}\text{Fe}_x$ layer (i) or in both layers (ii). The calculated exchange interaction parameters for these cases are presented in Fig. 6. For the case (i) and $x = 0.1$ the exchange parameter between the nearest neighbors is positive ($J_1^{00} = 1.75 \text{ meV}$), while the next nearest (NN) and next next nearest (NNN) neighbor interaction parameters are negative and comparable in magnitude with the nearest neighbor coupling: $J_2^{00} = -1.09 \text{ meV}$ and $J_3^{00} = -1.28 \text{ meV}$, respectively. According to the magnon spectrum calculations (not shown) this leads to a noncollinear magnetic structure with the wave vector $\vec{q} = (0.38, 0, 0) \text{ \AA}^{-1}$ while the critical temperature T_C is equal

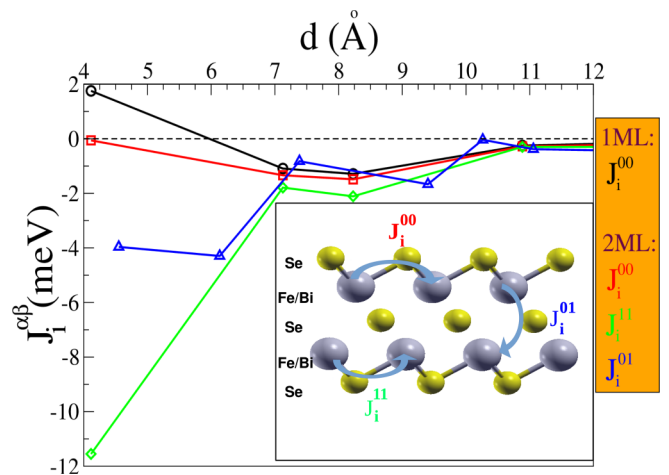


FIG. 6. (Color online) Calculated exchange interaction in $\text{Bi}_{1.9}\text{Fe}_{0.1}\text{Se}_3$ (Fe is only in the subsurface Bi layer) and $\text{Bi}_{1.8}\text{Fe}_{0.2}\text{Se}_3$ (Fe is in both Bi layers of the first QL). The inset shows the structure of the first quintuple layer with the corresponding exchange parameters indicated.

to 3.5 K, as estimated within the random phase approximation. A collinear AF structure corresponds to $\vec{q} = (0.76, 0, 0) \text{ \AA}^{-1}$. For $x = 0.2$ we found $T_C = 6.2 \text{ K}$, but the ordering vector \vec{q} has not changed.

The situation changes for the case (ii). Here, an AF *interlayer* coupling exists between the nearest neighbors: $J_1^{00} = -0.06 \text{ meV}$ for the subsurface layer and $J_1^{11} = -11.53 \text{ meV}$ in the second Bi layer ($x = 0.2$, i.e., 0.1 in each Bi layer). Also, the NN and NNN neighbor interactions retain their negative value (see Fig. 6). This increases the tendency to an AF order. However, the strength of the interaction is not sufficient to develop a compensated collinear AF order and the magnetic structure is noncollinear but with the wave vector $\vec{q} = (0.53, 0, 0) \text{ \AA}^{-1}$, i.e., closer to the collinear AF structure. The critical temperature of the structure was determined to be 8.1 K (10 K at $x = 0.4$ in the QL or 0.2 in each Bi layer).

V. SUMMARY

In summary we have presented a polarization-dependent EXAFS analysis of the structure of ultrathin iron film of 0.3 ML thickness deposited on the (0001) surface of Bi_2Se_3 at 160 K. We find that iron replaces bismuth atoms involving a substantial structural relaxation of the order of 0.4 \AA of the neighboring selenium atoms toward the iron atom. We find a dispersion of Fe-Se distances varying between 2.39 and 2.57 \AA , which is attributed to the inequivalence of the nearest neighbor selenium around bismuth atoms sites within a quintuple layer. No indication of interstitial or intercalated iron atoms has been found. For such a situation, our *ab initio* calculations predict a noncollinear order with a T_C in the range between 3.5 and 10.0 K. Finally, after mild annealing of the as-deposited sample up to 520 K for several minutes the EXAFS analysis gives evidence for the formation of a α -FeSe-like structure with a local order up to the 6th shell at a distance close to 6 \AA .

ACKNOWLEDGMENTS

We acknowledge financial support from DFG through priority program SPP1666 (Topological Insulators). Technical support by F. Weiss is gratefully acknowledged. We also thank Z. S. Aliev, M. B. Babanly, K. A. Kokh, and O. E. Tereshchenko for support by providing samples. M.M.O. and E.V.C. thank the Tomsk State University Academic D. I. Mendeleev Fund Program (Research Grant No. 8.1.05.2015). Partial support by the Saint Petersburg State University Project No. 11.50.202.2015 is also acknowledged. The calculations were performed at the Rechenzentrum Garching of the Max Planck Society (Germany), the SKIF-Cyberia supercomputer

of Tomsk State University, and DIPC computing center. E.D.C. acknowledges research grants from the Dean, Faculty of Science, Simon Fraser University, and from NSERC. Sector 20 facilities at the Advanced Photon Source, and research at these facilities, are supported by the US Department of Energy–Basic Energy Sciences, the Canadian Light Source and its funding partners, the University of Washington, and the Advanced Photon Source. Use of the Advanced Photon Source, an Office of Science User Facility operated for the US Department of Energy (DOE) Office of Science by Argonne National Laboratory, was supported by the US DOE under Contract No. DE-AC02-06CH11357.

-
- [1] M. Z. Hasan and C. L. Kane, *Rev. Mod. Phys.* **82**, 3045 (2010).
- [2] L. Fu, C. L. Kane, and E. J. Mele, *Phys. Rev. Lett.* **98**, 106803 (2007).
- [3] T. Zhang, P. Cheng, X. Chen, J.-F. Jia, X. Ma, K. He, L. Wang, H. Zhang, X. Dai, Z. Fang *et al.*, *Phys. Rev. Lett.* **103**, 266803 (2009).
- [4] P. Roushan, J. Seo, C. V. Parker, Y. S. Hor, D. Hsieh, D. Qian, A. Richardella, M. Z. Hasan, R. J. Cava, and A. Yazdani, *Nature (London)* **460**, 1106 (2009).
- [5] T. Hanaguri, K. Igarashi, M. Kawamura, H. Takagi, and T. Sasagawa, *Phys. Rev. B* **82**, 081305 (2010).
- [6] Y. Xia, D. Qian, D. Hsieh, L. Wray, A. Pal, H. Lin, A. Bansil, D. Grauer, Y. S. Hor, R. J. Cava *et al.*, *Nat. Phys.* **5**, 398 (2009).
- [7] H. Zhang, C.-X. Liu, X.-L. Qi, X. Dai, Z. Fang, and S.-C. Zhang, *Nat. Phys.* **5**, 438 (2009).
- [8] S. V. Eremeev, G. Landolt, T. V. Menshchikova, B. Slomski, Y. M. Koroteev, Z. S. Aliev, M. B. Babanly, J. Henk, A. Ernst, L. Patthey *et al.*, *Nat. Commun.* **3**, 635 (2012).
- [9] P. Sessi, M. M. Otrokov, T. Bathon, M. G. Vergniory, S. S. Tsirkin, K. A. Kokh, O. E. Tereshchenko, E. V. Chulkov, and M. Bode, *Phys. Rev. B* **88**, 161407 (2013).
- [10] P. Wei, F. Katmis, B. A. Assaf, H. Steinberg, P. Jarillo-Herrero, D. Heiman, and J. S. Moodera, *Phys. Rev. Lett.* **110**, 186807 (2013).
- [11] T. V. Menshchikova, M. M. Otrokov, S. S. Tsirkin, D. A. Samorokov, V. V. Bebnava, A. Ernst, V. M. Kuznetsov, and E. V. Chulkov, *Nano Lett.* **13**, 6064 (2013).
- [12] R. Shokri, H. L. Meyerheim, S. Roy, K. Mohseni, A. Ernst, M. M. Otrokov, E. V. Chulkov, and J. Kirschner, *Phys. Rev. B* **91**, 205430 (2015).
- [13] Z.-H. Zhu, G. Levy, B. Ludbrook, C. N. Veenstra, J. A. Rosen, R. Comin, D. Wong, P. Dosanjh, A. Ubaldini, P. Syers *et al.*, *Phys. Rev. Lett.* **107**, 186405 (2011).
- [14] H. M. Benia, C. Lin, K. Kern, and C. R. Ast, *Phys. Rev. Lett.* **107**, 177602 (2011).
- [15] P. D. C. King, R. C. Hatch, M. Bianchi, R. Ovsyannikov, C. Lupulescu, G. Landolt, B. Slomski, J. H. Dil, D. Guan, J. L. Mi *et al.*, *Phys. Rev. Lett.* **107**, 096802 (2011).
- [16] L. A. Wray, S.-Y. Xu, Y. Xia, D. Hsieh, A. V. Fedorov, Y. S. Hor, R. J. Cava, A. Bansil, H. Lin, and M. Z. Hasan, *Nat. Phys.* **7**, 32 (2011).
- [17] T. Valla, Z.-H. Pan, D. Gardner, Y. S. Lee, and S. Chu, *Phys. Rev. Lett.* **108**, 117601 (2012).
- [18] M. R. Scholz, J. Sánchez-Barriga, D. Marchenko, A. Varykhalov, A. Volykhov, L. V. Yashina, and O. Rader, *Phys. Rev. Lett.* **108**, 256810 (2012).
- [19] J. Honolka, A. A. Khajetoorians, V. Sessi, T. O. Wehling, S. Stepanow, J.-L. Mi, B. B. Iversen, T. Schlenk, J. Wiebe, N. B. Brookes *et al.*, *Phys. Rev. Lett.* **108**, 256811 (2012).
- [20] S. Roy, H. L. Meyerheim, A. Ernst, K. Mohseni, C. Tusche, M. G. Vergniory, T. V. Menshchikova, M. M. Otrokov, A. G. Ryabishchenkova, Z. S. Aliev *et al.*, *Phys. Rev. Lett.* **113**, 116802 (2014).
- [21] Q. Liu, C.-X. Liu, C. Xu, X.-L. Qi, and S.-C. Zhang, *Phys. Rev. Lett.* **102**, 156603 (2009).
- [22] D. A. Abanin and D. A. Pesin, *Phys. Rev. Lett.* **106**, 136802 (2011).
- [23] J. Henk, M. Flieger, I. V. Maznichenko, I. Mertig, A. Ernst, S. V. Eremeev, and E. V. Chulkov, *Phys. Rev. Lett.* **109**, 076801 (2012).
- [24] T. M. Schmidt, R. H. Miwa, and A. Fazzio, *Phys. Rev. B* **84**, 245418 (2011).
- [25] L. Chotorlishvili, A. Ernst, V. K. Dugaev, A. Komnik, M. G. Vergniory, E. V. Chulkov, and J. Berakdar, *Phys. Rev. B* **89**, 075103 (2014).
- [26] M. Ye, K. Kuroda, Y. Takeda, Y. Saitoh, K. Okamoto, S.-Y. Zhu, K. Shirai, K. Miyamoto, M. Arita, M. Nakatake *et al.*, *J. Phys.: Condens. Matter* **25**, 232201 (2013).
- [27] T. Schlenk, M. Bianchi, M. Koleini, A. Eich, O. Pietzsch, T. O. Wehling, T. Frauenheim, A. Balatsky, J.-L. Mi, B. B. Iversen *et al.*, *Phys. Rev. Lett.* **110**, 126804 (2013).
- [28] E. Wang, P. Tang, G. Wan, A. V. Fedorov, I. Miotkowski, Y. P. Chen, W. Duan, and S. Zhou, *Nano Lett.* **15**, 2031 (2015).
- [29] L. R. Shelford, T. Hesjedal, L. Collins-McIntyre, S. S. Dhesi, F. Maccherozzi, and G. van der Laan, *Phys. Rev. B* **86**, 081304 (2012).
- [30] M. Ye, S. V. Eremeev, K. Kuroda, E. E. Krasovskii, E. V. Chulkov, Y. Takeda, Y. Saitoh, K. Okamoto, S. Y. Zhu, K. Miyamoto *et al.*, *Phys. Rev. B* **85**, 205317 (2012).
- [31] D. West, Y. Y. Sun, S. B. Zhang, T. Zhang, X. Ma, P. Cheng, Y. Y. Zhang, X. Chen, J. F. Jia, and Q. K. Xue, *Phys. Rev. B* **85**, 081305 (2012).
- [32] C.-L. Song, Y.-P. Jiang, Y.-L. Wang, Z. Li, L. Wang, K. He, X. Chen, X.-C. Ma, and Q.-K. Xue, *Phys. Rev. B* **86**, 045441 (2012).

- [33] M. M. Yee, Z.-H. Zhu, A. Soumyanarayanan, Y. He, C.-L. Song, E. Pomjakushina, Z. Salman, A. Kanigel, K. Segawa, Y. Ando *et al.*, *Phys. Rev. B* **91**, 161306 (2015).
- [34] R. A. Gordon, E. D. Crozier, D.-T. Jiang, J. Shoults, B. Barg, and P. S. Budnik, *AIP Conf. Proc.* **882**, 887 (2007).
- [35] D. T. Jiang and E. D. Crozier, *Can. J. Phys.* **76**, 621 (1998).
- [36] B. Ravel and M. Newville, *J. Synchrotron Radiat.* **12**, 537 (2005).
- [37] M. Newville, *J. Synchrotron Radiat.* **8**, 322 (2001).
- [38] S. I. Zabinsky, J. J. Rehr, A. Ankudinov, R. C. Albers, and M. J. Eller, *Phys. Rev. B* **52**, 2995 (1995).
- [39] D. C. Koningsberger and R. Prins, *X-Ray Absorption* (John Wiley and Sons, New York, 1988).
- [40] E. A. Stern, B. A. Bunker, and S. M. Heald, *Phys. Rev. B* **21**, 5521 (1980).
- [41] S. Margadonna, Y. Takabayashi, M. McDonald, K. Kasperkiewicz, Y. Mizuguchi, Y. Takano, A. Fitch, E. Suard, and K. Prassides, *Chem. Commun.* **2008**, 5607 (2008).
- [42] R. S. Kumar, Y. Zhang, S. Sinogeikin, Y. Xiao, S. Kumar, P. Chow, A. L. Cornelius, and C. Chen, *J. Phys. Chem. B* **114**, 12597 (2010).
- [43] The unweighted residuum (R_u) is defined by $R_u = \sum |Y_{\text{obs}} - Y_{\text{calc}}| / \sum Y_{\text{obs}}$, where Y_{obs} and Y_{calc} are the experimental and calculated magnitudes of the peak selected in the FT of the $\chi(k)$ spectrum and the summation extends over all points in the window used to filter the peak.
- [44] T. Ressler, *J. Synchrotron Radiat.* **5**, 118 (1998).
- [45] B. Joseph, A. Iadecola, A. Puri, L. Simonelli, Y. Mizuguchi, Y. Takano, and N. L. Saini, *Phys. Rev. B* **82**, 020502 (2010).
- [46] L. B. Abdalla, L. Seixas, T. M. Schmidt, R. H. Miwa, and A. Fazzio, *Phys. Rev. B* **88**, 045312 (2013).
- [47] A. I. Figueroa, G. van der Laan, L. J. Collins-McIntyre, S.-L. Zhang, A. A. Baker, S. E. Harrison, P. Schön herr, G. Cibin, and T. Hesjedal, *Phys. Rev. B* **90**, 134402 (2014).
- [48] Z. Liu, X. Wei, J. Wang, H. Pan, F. Ji, F. Xi, J. Zhang, T. Hu, S. Zhang, Z. Jiang *et al.*, *Phys. Rev. B* **90**, 094107 (2014).
- [49] M. Bendele, C. Marini, B. Joseph, L. Simonelli, P. Dore, S. Pascarelli, M. Chikovani, E. Pomjakushina, K. Conder, N. L. Saini *et al.*, *J. Phys.: Condens. Matter* **25**, 425704 (2013).
- [50] C.-L. Song, Y.-L. Wang, Y.-P. Jiang, Z. Li, L. Wang, K. He, X. Chen, X.-C. Ma, and Q.-K. Xue, *Phys. Rev. B* **84**, 020503 (2011).
- [51] M.-X. Wang, C. Liu, J.-P. Xu, F. Yang, L. Miao, M.-Y. Yao, C. L. Gao, C. Shen, X. Ma, X. Chen *et al.*, *Science* **336**, 52 (2012).
- [52] J.-F. Ge, C. Liu, C.-L. Gao, D. Qian, Q.-K. Xue, Y. Liu, and J.-F. Jia, *Nat. Mater.* **14**, 285 (2014).
- [53] A. Cavallin, K. Novakoski Fischer, S. Manna, S. Ouazi, M. Ellguth, C. Tusche, H. L. Meyerheim, D. Sander, and J. Kirschner (unpublished).
- [54] S. Manna, R. Shokri, S. Meyerheim, H. L. Roy, K. Mohseni, A. Cavallin, V. Sevriuk, D. Sander, and J. Kirschner (unpublished).
- [55] M. Lüders, A. Ernst, W. M. Temmerman, Z. Szotek, and P. J. Durham, *J. Phys.: Condens. Matter* **13**, 8587 (2001).
- [56] P. Soven, *Phys. Rev.* **156**, 809 (1967).
- [57] B. L. Gyorffy, *Phys. Rev. B* **5**, 2382 (1972).
- [58] M. G. Vergniory, M. M. Otrokov, D. Thonig, M. Hoffmann, I. V. Maznichenko, M. Geilhufe, X. Zubizarreta, S. Ostanin, A. Marmodoro, J. Henk *et al.*, *Phys. Rev. B* **89**, 165202 (2014).